Macrotheranostic Probe with Disease-activated Near-infrared Fluorescence, Photoacoustic and Photothermal Signals for Imaging-guided Therapy

Zhen, Xu; Zhang, Jianjian; Huang, Jiaguo; Xie, Chen; Miao, Qingqing; Pu, Kanyi

2018

Zhen, X., Zhang, J., Huang, J., Xie, C., Miao, Q., & Pu, K. (2018). Macrotheranostic Probe with Disease-activated Near-infrared Fluorescence, Photoacoustic and Photothermal Signals for Imaging-guided Therapy. Angewandte Chemie International Edition, in press.

https://hdl.handle.net/10356/88773

https://doi.org/10.1002/anie.201803321

COMMUNICATION

Macrotheranostic Probe with Disease-activated Near-infrared Fluorescence, Photoacoustic and Photothermal Signals for Imaging-guided Therapy

Xu Zhen, Jianjian Zhang, Jiaguo Huang, Chen Xie, Qingqing Miao and Kanyi Pu*

Abstract: Theranostics provides opportunities for precision cancer therapy. However, theranostic probes that simultaneously turn on their diagnostic signal and pharmacological action in respond to targeted biomarker have been less exploited. We herein report the synthesis of a macrotheranostic probe that specifically turns on near-infrared fluorescence (NIRF), photoacoustic (PA) and photothermal signals in the presence of cancer-overexpressed enzyme for imaging-guided cancer therapy. Superior to the small-molecule counterpart probe, the macrotheranostic probe has ideal biodistribution and renal clearance, permitting passive targeting of tumor, in-situ activation of multimodal signals, and effective photothermal therapy. Our study thus provides a macromolecular approach towards activatable multimodal phototheranostics.

Theranostics that integrates diagnostic and therapeutic capabilities into a single entity possesses the potential to detect disease at early stage, assess the accumulation of therapeutic agents at disease site, and predict therapeutic outcome.[1] Thereby, theranostics provides opportunities for precision medicine.[2] However, because most existing systems simply combine therapeutic agents with imaging probes through nano-encapsulation, their diagnostic signals and pharmacological effect are always on.[3] Thus, the efficacy of such theranostic probes strongly relies on the concentration difference between disease tissue and normal tissues, which is inevitably interfered by false signals and compromised by side effect to normal tissues.[4]

Ideal theranostic probes should undergo intrinsic signal evolution accompanied by simultaneous initiation of pharmacological action only upon detecting targeted biomarker in living systems.[5] However, such activatable theranostic probes are rare. Until now, enzyme,[6a] pH,[6b] glutathione (GSH),[6c,6d] and reactive oxygen species (ROS)[6e] responsive activatable theranostic probes have been developed for cancer therapy, but those probes are limited to the simple design of combining activatable fluorescent probes with chemotherapy prodrugs.[6] In addition, activatable theranostic probes with photothermal therapy (PTT) capability have been less exploited, although PTT has the advantage of high spatial-temporal controllability and minimal invasiveness.[7]

Herein, we report the design and synthesis of an activatable macrotheranostic probe that specifically turns on near-infrared fluorescence (NIRF), photoacoustic (PA) and photothermal signals in the presence of cancer for imaging-guided therapy. The macrotheranostic probe (CyGal-P) is composed of D-galactose caged NIR hemicyanine dye (CyOH) linked with a long poly(ethylene glycol) (PEG) chain (Scheme 1a). The D-galactose caged moiety can be specifically cleaved at the glycosidic bond by β-Galactosidase (βGal), an overexpressed glycoside hydrolase enzyme in ovarian cancers; whereas, the PEG chain provides enhanced hydrophilicity for improved biodistribution.[8] Thus, CyGal-P is initially non-fluorescent and non-photoacoustic because CyOH is in a "caged" state with diminished electron-donating ability of the oxygen atom.[9] After systemic administration, CyGal-P passively targets the tumor and can be specifically activated by βGal to turn-on its NIRF/PA signals (Scheme 1b), allowing for cancer-activated imaging-guided PTT. Note that although some fluorescent probes have been reported to detect βGal, βGal-activated theranostic agents have not been developed.[10]

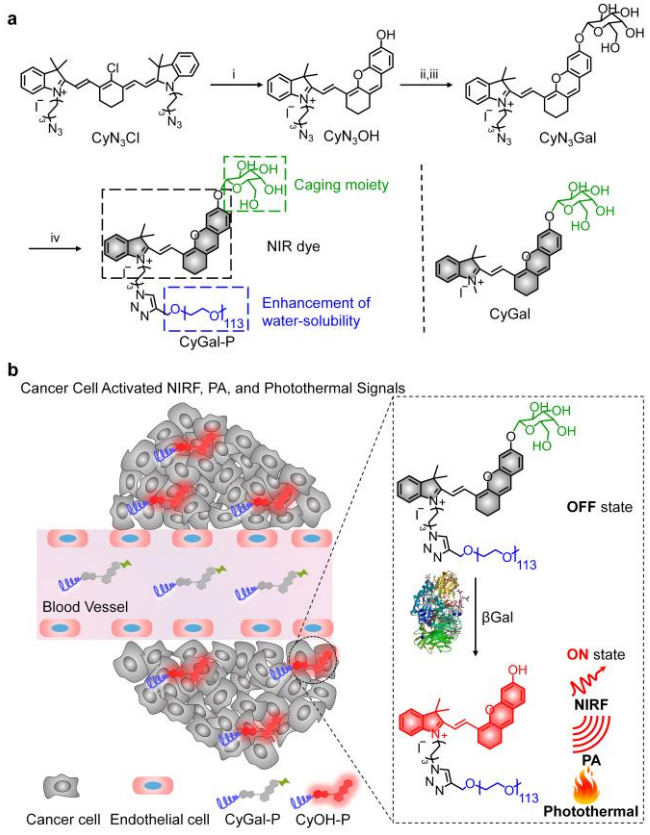

Scheme 1. (a) Synthesis of the macrotheranostic probe. Reagents and conditions: (i) tetra-O-acetyl-α-D-galactopyranosyl-1-bromide, Cs_2CO_3 / Na_2SO_4, MeCN, 80 °C, 12 h; (ii) MeONa, MeOH, 25 °C, 1 h; (iii) resorcinol, K_2CO_3, MeCN, 25 °C, 0.5 h; (iv) mPEG-alkyne, $CuSO_4{\cdot}5H_2O$, Sodium ascorbate, DMF, 25 °C, 24 h. (b) Schematic illustration of activation mechanism of the macrotheranostic probe in βGal overexpressing cancer cell.

Scheme 1a presents the synthetic route of the macrotheranostic probe (CyGal-P) and the control probe without PEG (CyGal). CyN_3Cl was first reacted with resorcinol to afford CyN_3OH, followed by caging the oxygen atom with a D-galactose to afford CyN_3Gal. The structures of CyN_3OH and CyN_3Gal were confirmed by proton nuclear magnetic resonance (^1H NMR) and electrospray ionization-mass spectrometry (ESI-MS) (Figures S1-4, Supporting Information). Then, the obtained CyN_3Gal was reacted with propargyl end-PEG (PEG-alkyne) via copper(I)-catalyzed alkyne-azide cycloaddition (CuAAC) reaction to obtain the final PEG conjugated CyGal (CyGal-P). The structure was confirmed by ^1H NMR (Figure S5, Supporting Information). The control probe CyGal was synthesized from CyOH by caging the oxygen atom with a D-galactose (Figure S6, Supporting

Information). The structure was confirmed by ^{1}H NMR and ESI-MS (Figures S7&8, Supporting Information).

To test the probe response toward βGal, the optical properties of CyGal-P and CyGal in the absence or presence of βGal were studied and compared. Initially, both CyGal-P and CyGal had the absorption maximum at 600 nm and were nonfluorescent. After incubation with βGal, both probes showed obvious decrease in the absorption peak at 600 nm (Figure 1a), concomitant with the appearance of a new peak at 688 nm corresponding to CyOH. The absorption intensities at 688 nm were quantified as a function of incubation time (Figure S9a&c, Supporting Information). CyGal-P showed gradually increased absorption intensity at 688 nm with increased incubation time, and reached plateau at 40 min. However, the absorption intensity of CyGal at 688 nm reached maximum at 15 min and then decreased with increased incubation time. This should be caused by the poor water-solubility of CyGal after βGal cleavage, as the tiny precipitation was observed. The absorption intensities at 688 nm of both CyGal-P and CyGal were dramatically decreased when βGal was treated with the competitive inhibitor (D-(+)-Galactose) of βGal, demonstrating the high selectivity towards βGal (Figure 1a). In addition, after incubation with βGal, CyGal-P and CyGal showed dramatically increased fluorescence with the maximum peak at 720 and 712 nm, respectively (Figure 1b). Due to the poor water solubility, the fluorescence intensity of CyGal only showed 24-fold enhancement, which was nearly 2-times lower than for CyGal-P (47-fold) (Figure S9b&d, Supporting Information). Such fluorescence change was not observed for both probes in the prescence of the inhibitor (D-(+)-Galactose) (Figure 1b). High performance liquid chromatography (HPLC) analysis further showed that CyGal-P and were completely cleaved (Figure S10, Supporting Information). The enzymatic Michaelis-Menten constants (K_m) and the catalytic rate constants (K_{cat}) of βGal towards CyGal-P and CyGal were calculated to be 48.3 μM and 30.85 s^{-1} for CyGal-P, and 66.8 μM and 54.16 s^{-1} for CyGal (Figure S11, Supporting Information), Therefore, the catalytic efficiencies (K_{cat}/K_m) of βGal towards CyGal-P and CyGal was calculated to be 6.39 × 10^5 and 8.11 × 10^5 M^{-1} s^{-1}, respectively. These data proved that βGal could efficiently induce the cleavage of both probes, and CyGal-P showed much higher fluorescence enhancement relative to CyGal.

The PA and photothermal properties of the macrotheranostic probe (CyGal-P) were studied and compared with CyGal. The PA spectra of CyGal-P and CyGal in the absence or presence of βGal were close to their absorption spectra ranging from 680 to 850 nm (Figure 1c). In the presence of βGal, the PA signals of both probes at 680 nm significantly increased, but the signal of CyGal-P was 1.8-times higher than that of CyGal (Figure 1c inset). This was consistent with the absorption increase at 680 nm upon treatment with βGal. Furthermore, the photothermal properties of CyGal-P and CyGal in the absence or presence of βGal also showed the similar tendency (Figure 1d). Under continuous laser irradiation at 680 nm, CyGal-P and CyGal treatment with βGal showed gradually increased temperatures and reached plateau at t = 180 s; in contrast, the temperatures without βGal barely showed increase due to the low absorption of the inactivated probes at 680 nm. The maximum photothermal temperatures of βGal-activated CyGal-P and CyGal were 48 and 37 °C, respectively (Figure S12a, Supporting Information). The reversible heating-cooling operation showed that βGal-activated CyGal-P remained nearly the same for at least 5 cycles, while βGal-activated CyGal failed to do so (Figure S12b, Supporting Information). The absorption spectra before and after light irradiation revealed that the absorption at 688 nm dramatically decreased for CyGal but remained nearly the same for CyGal-P (Figure S12c&d, Supporting Information). This indicated that the presence of PEG also enhanced the photothermal stability of uncaged NIR dye, which was probably due to the faster heat dissipation of well-dissolved dye relative to the aggregated dye. These data confirmed that the macrotheranostic probe activated its PA and photothermal signals in the presence of βGal.

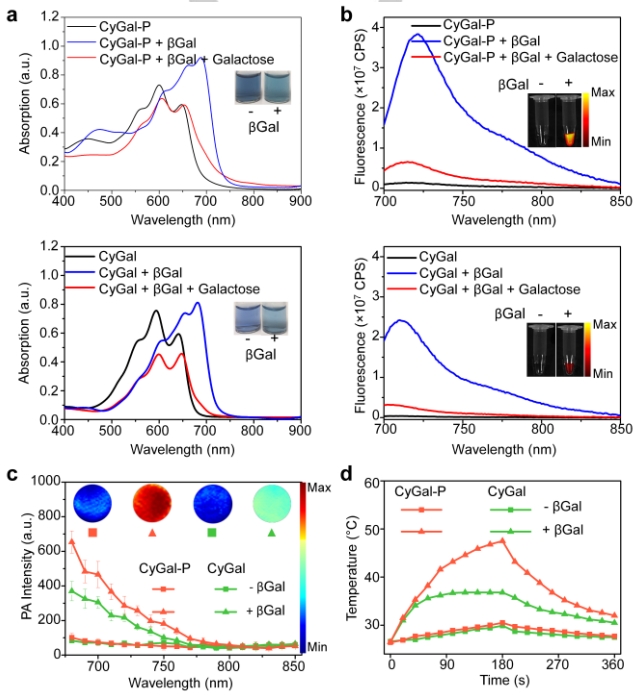

Figure 1. UV-Vis absorption spectra (a) and fluorescence (b) of CyGal-P (top) or CyGal (down) (30 μM) in the absence or presence of βGal (0.6 U mL^{-1}) at 37 °C in HEPES buffer (100 mM, pH = 7.4) containing 5% (V/V) DMSO, 1mM $MgCl_2$, and 100mM mercaptoethanol, D-(+)-Galactose (inhibitor) (1 mM) with βGal (0.6 U mL^{-1}) in HEPES buffer (100 mM, pH = 7.4). Excitation: 680 nm. Inset: white light (a) and fluorescence images (b) of CyGal-P (top) or CyGal (down) (30 μM) in the absence or presence of βGal (0.6 U mL^{-1}) for 40 min at 37 °C in HEPES buffer. The fluorescence images were acquired at 720 nm upon excitation at 675 nm. (c) The PA spectra of CyGal and CyGal-P (30 μM) in the absence or presence of βGal (0.6 U mL^{-1}) for 40 min at 37 °C in HEPES buffer (100 mM, pH = 7.4) containing 5% (V/V) DMSO, 1mM $MgCl_2$, and 100mM ercaptoethanol. Inset: The PA images of CyGal and CyGal-P (30 μM) in the absence or presence of βGal (0.6 U mL^{-1}). (d) The temperature of CyGal and CyGal-P (30 μM) in the absence or presence of βGal (0.6 U mL^{-1}) as a function of laser irradiation time. The laser irradiation wavelength was at 680 nm with a power of 0.6 W cm^{-2}.

To test the response of the macrotheranostic probe CyGal-P toward βGal in cells, the fluorescence imaging was conducted on the βGal-overexpressed ovarian cancer cells (SKOV3) and the control cells (NIH-3T3). Strong NIR fluorescence signals for both CyGal-P and CyGal treated SKOV3 cells were detected after 1 h incubation (Figure S13a, Supporting Information). However, the fluorescence for CyGal-P treated SKOV3 cells was ~2.1-fold of that for CyGal treated SKOV3 cells (Figure S13b, Supporting

Information), consistent with the solution results. In contrast, the fluorescence signals were barely observed for NIH-3T3 cells after probe treatment (Figure S13a, Supporting Information). These results confirmed the macrotheranostic probe was specifically activated by βGal with better signal response relative to the control probe.

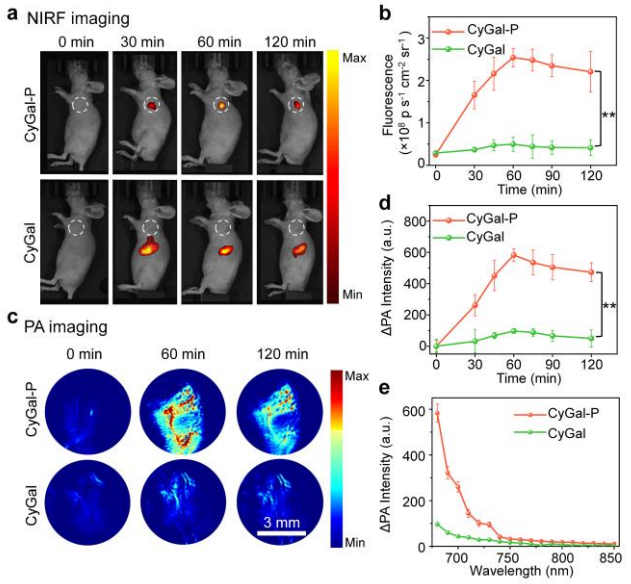

Figure 2. In vivo tumor NIRF and PA imaging of the macrotheranostic probe CyGal-P. (a) Representative fluorescence images of SKOV3 tumor-bearing living mice at different time points after intravenous injection of CyGal-P or CyGal (300 μM). (b) Quantification of fluorescence intensities of tumor as a function of post-injection time of CyGal-P or CyGal. (c) Representative PA images of SKOV3 tumor-bearing living mice at different time points after intravenous injection of CyGal-P or CyGal (300 μM). (d) PA intensity increment at 680 nm (ΔPA680) of tumor as a function of post-injection time of CyGal-P or CyGal in SKOV3 tumor-bearing living mice. (e) In vivo real-time PA intensity increment spectra of tumor areas after intravenous administration of CyGal-P or CyGal at 60 min. Double asterisks indicate $P < 0.01$.

To examine the PTT efficacy of the macrotheranostic probe in vitro, SKOV3 cells were incubated with CyGal-P or CyGal for 1 h and then irradiated for 5 min with a 680 nm laser (0.6 W cm^{-2}). The cell status was qualitatively evaluated by calcein AM (live cells, green fluorescence) and propidium iodide (dead cells, red fluorescence) staining (Figure S14, Supporting Information), as well as quantitatively measured by using 3-(4,5-dimethylthiazol-2-yl)-5-(3-carboxymethoxyphenyl)-2-(4-sulfophenyl)-2H-tetrazolium (MTS) assays (Figure S15, Supporting Information). Both CyGal-P and CyGal had no obvious cytotoxicity without laser irradiation. Due to the efficient cleavage of CyGal-P and better photothermal stability after βGal activation, high temperature (48 °C) were achieved to ablate almost all the SKOV3 cells under laser irradiation (Figure 1d, Figure S14 and Figure S15, Supporting Information). In contrast, CyGal failed to do so.

To evaluate the in vivo biodistribution of probes, CyGal-P and CyGal were respectively injected into living mice via intravenous injection (Figure S16, Supporting Information). Although the CyGal-P and CyGal showed weak fluorescence (Figure 1b), the detectable NIRF signals attributed to CyGal-P and CyGal could represent the in vivo biodistribution of the probes. CyGal-P was found to have higher accumulation in kidneys, and could be cleared out through renal excretion, while CyGal was mainly accumulated in liver. These data revealed that the enhanced water-solubility of the macrotheranostic probe (CyGal-P) helped the escape from mononuclear phagocytic system (MPS) and facilitated renal clearance.[11]

The in vivo tumor NIRF and PA imaging capability of the macrotheranostic probe (CyGal-P) was tested in the subcutaneous SKOV3 xenograft tumor model. After systemic administration of CyGal-P or CyGal into the living mice through tail vein, both NIRF and PA images were longitudinally recorded and quantified (Figures 2a-d). The NIRF and PA intensities gradually increased for CyGal-P over time and reached peak at 60 min post-injection, indicating that CyGal-P could efficiently accumulate in tumor region and undergo cleavage by βGal overexpressed in SKOV3 cells. In contrast, due to the poor water-solubility, CyGal showed very low accumulation in tumor region, failing to delineate tumor. The in vivo PA spectrum of the tumor from the CyGal-P treated mice resembled the solution spectrum of βGal-activated CyGal-P (Figure 1c and figure 2e), while the spectrum of the tumor from the CyGal treated mice was similar to the background. These data verified that the increased PA signals in tumor region came from βGal-activated CyGal-P.

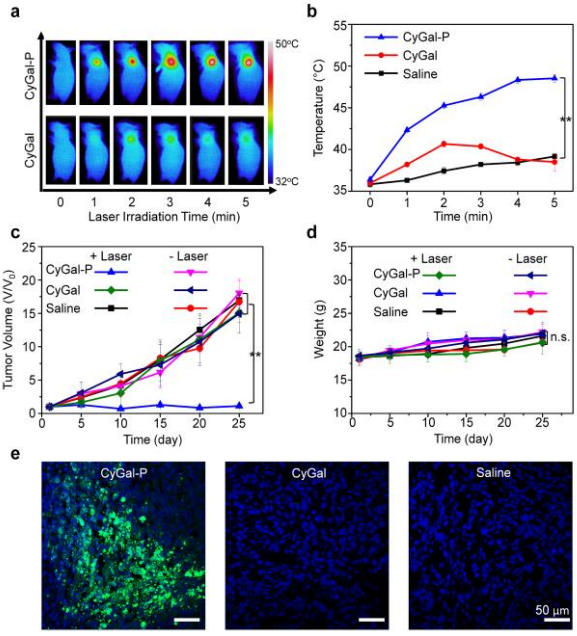

Figure 3. In vivo PTT of the macrotheranostic probe CyGal-P. (a) IR thermal images of SKOV3 tumor-bearing mice under laser irradiation at 680 nm (0.6 W cm^{-2}) for different time after intravenous injection of CyGal and CyGal-P (300 μM). (b) Mean tumor temperature during laser irradiation after intravenous injection of saline, CyGal and CyGal-P (300 μM) into SKOV3 tumor-bearing mice. Error bars were based on standard error of mean (SEM) (n = 4). (c) Tumor growth curves and (d) body weight data of mice after intravenous injection of saline, CyGal and CyGal-P (300 μM) into SKOV3 tumor-bearing mice with or without laser irradiation at 680 nm (n = 4). (e) Immunofluorescent staining of caspase-3 for tumors on mice treated with saline, CyGal and CyGal-P (300 μM) with laser irradiation. Green fluorescence indicates the signal from caspase-3 staining, while blue fluorescence indicates nucleus staining. The tumors for immunofluorescent staining were collected after 25 days of treatment. Double asterisks indicate $P < 0.01$. n.s. indicates no statistically significant differences.

Because CyGal-P had the highest activated NIRF and PA signals in tumor region at 60 min post-injection, PTT was conducted at this time point. The SKOV3-tumor bearing mice were irradiated at 680 nm (0.6 W cm^{-2}) for 5 min. The tumor temperature for CyGal-P treated mice gradually increased and reached plateau at 4 min, which was significantly higher than that for both CyGal and saline treated mice at all the time points (Figure 3a&b). The tumor temperature for CyGal treated mice reached maximum at 2 min and then dropped due to the decomposition of CyGal during the laser irradiation (Figure S12 c, Supporting Information). The maximal tumor temperature of CyGal-P treated mice was 48.3°C, which was ~9.5 and 9.3 °C higher than that of CyGal and saline treated mice. These data indicated that the amount of βGal-activated CyGal-P in tumor was higher enough to induce the photothermal heating above the threshold temperature (43 °C) for cellular ablation, which is impossible for CyGal.[12]

To qualitatively investigate the PTT efficacy of the macrotheranostic probe, the growth rates of tumors were continuously monitored after PTT treatments (Figure 3c). CyGal-P successfully suppressed the tumor growth after PTT, while CyGal failed to do so (Figure S17, Supporting Information). This was attributed to the fact that CyGal-P had higher accumulation in tumor and led to higher photothermal temperature. No therapeutic effect was found for all the groups without laser irradiation. Moreover, no significant weight loss in the mice for all groups was observed for 25 days after PTT (Figure 3d), and no noticeable histopathological abnormalities was found in livers, kidneys, and spleens (Figure S18, Supporting Information), showing the good biosafety of both probes. Immunofluorescence caspase-3 staining images revealed that a large fraction of green fluorescence spots were observed for the tumor tissues of CyGal-P treated mice after PTT (Figure 4e), while no green fluorescence spots were found for other control groups (Figure S19, Supporting Information), indicating only CyGal-P mediated PTT led to the severe cellular apoptosis.[13] Therefore, these data verified that the macrotheranostic probe had a specific PTT efficacy and minimal toxicity to normal tissues.

In conclusion, we synthesized a macrotheranostic probe (CyGal-P) that can be specifically activated by an ovarian cancer overexpressed enzyme (βGal) to turn on its NIRF, PA and photothermal signals for imaging-guided cancer therapy. Thus, CyGal-P is different from the most reported theranostics agents whose signal and pharmacological action are always on.[3] Moreover, as compared with the small-molecule counterpart probe (CyGal), CyGal-P showed significantly higher fluorescence (47-fold vs 24-fold), PA (654 vs 370), and photothermal (48 °C vs 37 °C) enhancement after activation by βGal. With the help of hydrophilic PEG, CyGal-P also had the ideal biodistribution with renal clearance and passive accumulation in tumor, which was not possible for CyGal. As a result, only CyGal-P could delineate the tumor with both NIRF and PA imaging and activate its photothermal heat to ablate the βGal-overexpressed ovarian cancer cells (SKOV3) in living mice after systemic administration. To the best of our knowledge, our study represents the first example of activatable phototheranostic agent with multimodal imaging and PTT capabilities.

Acknowledgements

K.P. thanks Nanyang Technological University (Start-Up grant: NTUSUG: M4081627.120) and Singapore Ministry of Education (Academic Research Fund Tier 1: RG133/15 M4011559 and 2015-T1-002-091; and Tier 2 MOE2016-T2-1-098) for the financial support.

Conflict of interest

The authors declare no conflict of interest.

Keywords: activatable macrotheranostic probe • β-Galactosidase • near-infrared fluorescence imaging • photoacoustic imaging • photothermal therapy

[1] a) G. M. Lanza, *Nat. Nanotechnol.* **2015**, *10*, 301; b) C. Li, *Nat. Mater.* **2014**, *13*, 110-115; c) S. A. Chechetka, Y. Yu, X. Zhen, M. Pramanik, K. Pu, E. Miyako, *Nat. Commun.* **2017**, *8*, 15432; d) R. Kumar, W. S. Shin, K. Sunwoo, W. Y. Kim, S. Koo, S. Bhuniya, J. S. Kim, *Chem. Soc. Rev.* **2015**, *44*, 6670-6683.

[2] a) S.-m. Park, A. Aalipour, O. Vermesh, J. H. Yu, S. S. Gambhir, *Nat. Rev. Mater.* **2017**, *2*, 17014; b) K. Yang, L. Feng, X. Shi, Z. Liu, *Chem. Soc. Rev.* **2013**, *42*, 530-547; c) J. H. Ryu, S. Lee, S. Son, S. H. Kim, J. F. Leary, K. Choi, I. C. Kwon, *J. Control. Release* **2014**, *190*, 477-484; d) Y. Lyu, Y. Fang, Q. Miao, X. Zhen, D. Ding, K. Pu, *ACS Nano* **2016**, 10, 4472-4481.

[3] a) K. K. Ng, J. F. Lovell, G. Zheng, *Accounts Chem. Res.* **2011**, *44*, 1105-1113; b) J. V. Jokerst, S. S. Gambhir, *Accounts Chem. Res.* **2011**, *44*, 1050-1060; c) H. Huang, J. F. Lovell, *Adv. Funct. Mater.* **2017**, *27*; d) Z. Zhou, K. Hu, R. Ma, Y. Yan, B. Ni, Y. Zhang, L. Wen, Q. Zhang, Y. Cheng, *Adv. Funct. Mater.* **2016**, *26*, 5971-5978; e) Y. Jiang, D. Cui, Y. Fang, X. Zhen, P.K. Upputuri, M. Pramanik, D. Ding, K. Pu, *Biomaterials*, **2017**, 145, 168-177.

[4] a) Y. Chen, L. Cheng, Z. Dong, Y. Chao, H. Lei, H. Zhao, J. Wang, Z. Liu, *Angew. Chem. Int. Ed.* **2017**, 56, 12991-12996; *Angew. Chem.* **2017,** *129*, 13171-13176; b) D. Y. Lee, J. Y. Kim, Y. Lee, S. Lee, W. Miao, H. S. Kim, J. J. Min, S. Jon, *Angew. Chem. Int. Ed.* **2017**, *56*, 13684-13688; *Angew. Chem.* **2017**, *129*, 13872-13876.

[5] a) E.-K. Lim, T. Kim, S. Paik, S. Haam, Y.-M. Huh, K. Lee, *Chem. Rev.* **2014**, *115*, 327-394; b) C. Yin, X. Zhen, Q. Fan, W. Huang, K. Pu, *ACS Nano*, **2017**,11,4174-4182; c) J. Zhang, X. Zhen, P.K. Upputuri, M. Pramanik, P. Chen, K. Pu, *Advanced Materials*, **2017**, 29, 1604764.

[6] a) S. Bhuniya, S. Maiti, E. J. Kim, H. Lee, J. L. Sessler, K. S. Hong, J. S. Kim, *Angew. Chem. Int. Ed.* **2014**, *53*, 4469-4474; *Angew. Chem.* **2014**, *126*, 4558-4563; b) S.-M. Lee, Y. Song, B. J. Hong, K. W. MacRenaris, D. J. Mastarone, T. V. O'Halloran, T. J. Meade, S. T. Nguyen, *Angew. Chem. Int. Ed.* **2010**, *49*, 9960-9964; Angew. Chem. **2010**, *122*, 10156-10160; c) J. Wu, L. Zhao, X. Xu, N. Bertrand, W. I. Choi, B. Yameen, J. Shi, V. Shah, M. Mulvale, J. L. MacLean, *Angew. Chem. Int. Ed.* **2015**, *54*, 9218-9223; *Angew. Chem.* **2015,** *127*, 9350-9355; d) S. Santra, C. Kaittanis, O. J. Santiesteban, J. M. Perez, *J. Am. Chem. Soc.* **2011**, *133*, 16680-16688; e) R. Kumar, J. Han, H.-J. Lim, W. X. Ren, J.-Y. Lim, J.-H. Kim, J. S. Kim, *J. Am. Chem. Soc.* **2014**, *136*, 17836-17843;

[7] a) T. D. MacDonald, T. W. Liu, G. Zheng, *Angew. Chem. Int. Ed.* **2014**, *53*, 6956-6959; *Angew. Chem.* **2014**, *126*, 7076-7079; b) B. Wu, S.-T. Lu, H. Yu, R.-F. Liao, H. Li, B. L. Zafitatsimo, Y.-S. Li, Y. Zhang, X.-L. Zhu, H.-G. Liu, H.-B. Xu, S.-W. Huang, Z. Cheng, *Biomaterials* **2017**, *159*, 37-47; c) X. Zhen, C. Xie, Y. Jiang, X. Ai, B. Xing, K. Pu, *Nano Lett.* **2018**, *18*, 1498-1505; d) X. Zhen, C. Xie, K. Pu, *Angew. Chem. Int. Ed.* **2018**, *57*, 3938-3942.; *Angew. Chem.* **2018**, *130*, 4002-4006; e) W. Tao, X. Ji, X. Xu, M. Ariful Islam, Z. Li, S. Chen, P. E. Saw, H. Zhang, Z. Bharwani, Z. Guo, J. Shi, O. C. Farokhzad, *Angew. Chem. Int. Ed.* **2017**, *56,* 11896-11900; *Angew. Chem.* **2017**, *129*, 12058-12062.

[8] a) D. Asanuma, M. Sakabe, M. Kamiya, K. Yamamoto, J. Hiratake, M. Ogawa, N. Kosaka, P. L. Choyke, T. Nagano, H. Kobayashi, *Nat. Commun.* **2015**, *6*, 6463; b) K. Gu, Y. Xu, H. Li, Z. Guo, S. Zhu, S. Zhu, P. Shi, T. D. James, H. Tian, W.-H. Zhu, *J. Am. Chem. Soc.* **2016**, *138*, 5334-5340.

[9] Q. Miao, D. C. Yeo, C. Wiraja, J. Zhang, X. Ning, C. Xu, K. Pu, *Angew. Chem. Int. Ed.* **2018**, *57*, 1256-1260; *Angew. Chem.* **2018**, *130*, 1270-1274.

[10] a) B. Lozano-Torres, I. Galiana, M. Rovira, E. Garrido, S. Chaib, A. Bernardos, D. Muñoz-Espín, M. Serrano, R. Martínez-Máñez, F. Sancenón, *J. Am. Chem. Soc.* **2017**, *139*, 8808-8811; b) T. S. Wehrman, G. von Degenfeld, P. O. Krutzik, G. P. Nolan, H. M. Blau, *Nat. Methods* **2006**, *3*, 295, c) J. Zhang, C. Li, C. Dutta, M. Fang, S. Zhang, A. Tiwari, T. Werner, F.-T. Luo, H. Liu, *Anal. Chim. Acta.* **2017**, *968*, 97-104.

[11] J. M. Harris, R. B. Chess, *Nat. Rev. Drug Discov.* **2003**, *2*, 214-221.

[12] B. Hildebrandt, P. Wust, O. Ahlers, A. Dieing, G. Sreenivasa, T. Kerner, R. Felix, H. Riess, *Crit. Rev. Oncol. Hematol.* **2002**, *43*, 33-56.

[13] J. R. Melamed, R. S. Edelstein, E. S. Day, *ACS Nano* **2015**, *9*, 6-11.

Entry for the Table of Contents (Please choose one layout)

Layout 1:

COMMUNICATION

Disease-activated near-infrared fluorescence, photoacoustic and photothermal signals for imaging-guided therapy: An activatable macrotheranostic probe is designed for imaging-guided photothermal therapy. The macrotheranostic probe could specifically turn on near-infrared fluorescence (NIRF), photoacoustic (PA) and photothermal signals in the presence of cancer-overexpressed enzyme (β-Galactosidase, βGal) for imaging-guided cancer therapy.

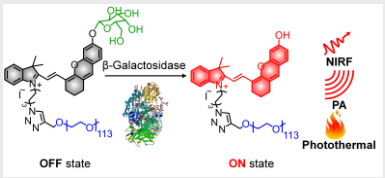

*Xu Zhen, Jianjian Zhang, Jiaguo Huang, Chen Xie, Qingqing Miao and Kanyi Pu**

Page No. – Page No.

Macrotheranostic Probe with Disease-activated Near-infrared Fluorescence, Photoacoustic and Photothermal Signals for Imaging-guided Therapy

Layout 2:

COMMUNICATION

*Author(s), Corresponding Author(s)**

Page No. – Page No.

Title

Text for Table of Contents